Single and triple differential cross sections for double photoionization of H^-

F. L. Yip,[1,4] D. A. Horner,[2] C. W. McCurdy,[3,4] and T. N. Rescigno[4]
[1]*Department of Chemistry, University of California, Berkeley, California 94720, USA*
[2]*Theoretical Division, Los Alamos National Laboratory, Los Alamos, New Mexico 87545, USA*
[3]*Department of Applied Science and Department of Chemistry, University of California, Davis, California 95616, USA*
[4]*Chemical Sciences, Lawrence Berkeley National Laboratory, Berkeley, California 94720, USA*
(Received 16 February 2007; published 24 April 2007)

The hydride anion H^- would not be bound in the absence of electron correlation. Since the double-photoionization process is exquisitely sensitive to electron correlation, one expects electron correlation effects to leave a strong signature on the double-ionization cross sections for H^-. We present fully differential cross sections for the three-body breakup of H^- by single-photon absorption. The absolute triply and singly differential cross sections were obtained from *ab initio* calculations making use of exterior complex scaling within a discrete-variable-representation partial-wave basis. Results calculated at photon energies of 18 and 30 eV are compared with reported cross sections for helium calculated at 20 eV above the double-ionization threshold. These comparisons show a clear signature of initial-state correlations that differentiate the He and H^- cases.

DOI: 10.1103/PhysRevA.75.042715 PACS number(s): 32.80.Gc

I. INTRODUCTION

Recent experimental investigations have focused on double photoionization (DPI) of two-electron atoms [1–7] and molecules [8–11] as a sensitive probe of the correlated motion of electrons. The DPI problem is interesting from both experimental and theoretical viewpoints because the process by which an atom or molecule absorbs a photon of sufficient energy to eject two electrons into the continuum necessarily depends on electron correlation. Since the optical absorption is described by a sum of one-body dipole operators, any theoretical approach that treats the electrons in an independent particle model with orthogonal orbitals will produce a zero result for the amplitudes connecting the initial and final states. Such considerations have been previously addressed using different theoretical approaches for both atomic [12–25] and molecular [26–30] two-electron targets, with varying degrees of electron correlation being included in the initial and/or final states.

In addition to providing a fingerprint of correlated electronic motion, double-photoionization problems represent an ambitious theoretical challenge because of the difficulty in applying the correct boundary conditions when two electrons enter the continuum. Since the pioneering theoretical work of the 1960s [31–33] to describe the correct asymptotic form of the wave function and the accompanying double ejection amplitude, numerous efforts have been applied to the more general three-body Coulomb breakup problem, including the use of ansatz wave functions [12–14], convergent close-coupling (CCC) methods [15–18], adapted *R*-matrix techniques [19,20], time-dependent close-coupling (TDCC) methods [21–23], complex basis functions [24], and finally the method of exterior complex scaling (ECS) [25,34,35]. In addition to ensuring that the calculated wave functions maintain the proper boundary conditions for three-body breakup, each method requires a proper means to extract the physically relevant amplitude associated with the two-electron outgoing wave to produce cross sections that can be compared with experiment.

The canonical system for both double-photoionization experimental investigations and theoretical calculations is the helium atom. This case represents a three-body Coulomb problem where electron repulsion represents a significant contribution to the energetics of the system. Theoretical treatments of helium DPI also benefit from atomic selection rules that restrict the overall final state produced from ground-state ^1S helium to ^1P symmetry, thereby restricting the number of coupled angular momentum contributions that must be considered in any partial wave expansion of the total wave function.

Analogous to the helium case is double photoionization of the isoelectronic hydride anion H^-. Indeed, from a theoretical point of view, DPI of H^- is more interesting because of the greater importance of electron repulsion relative to the Coulomb attraction of the electrons to the nucleus when $Z=1$. Thus, the atomic properties of H^- are more sensitive to electron correlation effects when compared to helium. This can be most easily demonstrated by simply comparing the results of a Hartree-Fock calculation of the He and H^- ground-state energies. Whereas in the case of helium the ground-state correlation energy is a few percent of the exact total energy, the Hartree-Fock energy of the hydride anion is above that of a $1s$ hydrogen atom and a free electron by 0.33 eV [36,37]. The fact that an independent electron treatment yields increasingly more significant contributions to the exact energy of atoms as the nuclear charge Z increases indicates that the electron correlation effects should be most important in the prototypical case of H^-.

Numerous theoretical approaches have been applied to double photoionization of H^-, dating back to a multichannel *J*-matrix calculation by Broad and Reinhardt [38]. Since then, the problem has been treated by model calculations [39,40], variational methods [41], *R*-matrix methods [42], convergent close coupling [43], time-dependent close-coupling [44], and most recently by wave-packet propagation [45]. The application of these various methods has yielded absolute total cross sections for DPI of H^- as well as ratios of single ionization to double ionization. However, the

most detailed information concerning angular distributions and ejected electron energy sharing has yet to be reported. In this paper, we complete the picture by applying the method of exterior complex scaling to calculate the two-electron outgoing wave function and the associated scattering amplitudes in order to report triply differential cross sections (TDCSs) for H^-. We will demonstrate, using our converged calculations and comparisons between H^- and helium, that a clear signature of initial-state correlation is revealed in the TDCS at extreme unequal energy sharing between the ejected photoelectrons, while near equal energy kinematics, the differences are less prominent.

First, we present a brief overview of exterior complex scaling and describe its application to a partial wave decomposition of the outgoing wave function, highlighting the extraction of double-photoionization amplitudes from the calculated solution. In Sec. III we present total cross sections of DPI of H^- and compare with previously reported calculated results. This is followed by singly and triply differential cross sections calculated at 18 and 30 eV photon energies, with our focus in the discussion being comparison of the present results with a similar treatment of the helium DPI case [25].

II. THEORETICAL FRAMEWORK

A. Exterior complex scaling approach

The details of using exterior complex scaling [46,47] in theoretical treatments of problems involving two or more continuum electrons have been extensively discussed in a recent review [35]. The method has been successful in providing essentially exact results for both electron-impact ionization of atomic hydrogen [34] and double photoionization of atomic [25] and molecular two-electron targets [27–29]. Here we present the main broad strokes that illustrate how ECS successfully deals with problems involving more than one continuum electron.

Exterior complex scaling avoids the difficulties associated with the explicit asymptotic form of multiparticle ejection wave functions mentioned above by imposing outgoing wave boundary conditions through a transformation of the radial coordinate of the ejected particles,

$$r \to \begin{cases} r, & r \le R_0, \\ R_0 + (r - R_0)e^{i\theta}, & r > R_0, \end{cases} \tag{1}$$

where R_0 defines a radius beyond which the coordinates of each electron become complex-scaled by a scaling angle θ. This rotation of r into the complex plane is illustrated in Fig. 1, where the radial coordinate before R_0 corresponds to physical values. As previously discussed [35], this transformation avoids the difficulties associated with explicitly imposing proper boundary conditions by causing solutions with purely outgoing waves to decay exponentially along the complex-scaled contour. This is demonstrated in the lower panel of Fig. 1, which shows the exponential damping effect of complex scaling beyond R_0=20 on the one-dimensional outgoing wave function for a model problem [48]. Because of the sharp rotation of the radial coordinate into the complex plane at R_0, the wavefunction itself develops a discontinuous first derivative across this turning point. Several adapted techniques for describing the radial coordinate, including the use of finite elements [34], B splines [48], and the discrete-variable representation [49], have been employed to address the issues associated with exterior complex scaling. It is important to note that inside R_0 the wave function corresponds to the physical solution, thus allowing the calculation of amplitudes associated with processes involving electron ejection, provided that the purely real part of the grid is large enough to allow the wave function to reach its asymptotic form. We briefly summarize the extraction of relevant DPI amplitudes calculated within the ECS framework in the following section.

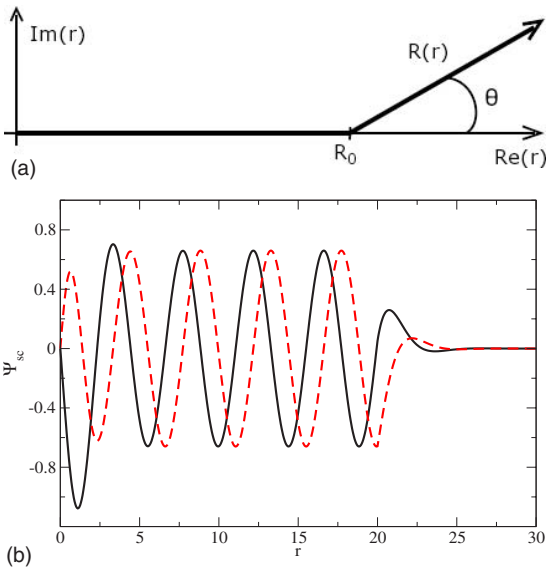

FIG. 1. (Color online) Exterior complex scaling in a single radial dimension. (a) ECS contour in the complex plane, demonstrating the rotation of the radial coordinate beyond R_0 into the upper half complex plane by angle θ. (b) Real (solid line) and imaginary (dashed line) components of an outgoing wave solution (in arbitrary units) for a model problem [48] along the ECS contour. The oscillatory nature of the outgoing waves is exponentially damped by the coordinate transformation beyond R_0. Inside R_0 the outgoing wave is the physical solution. The radial coordinate r is plotted in atomic units.

B. Formulation of the atomic double-photoionization problem

The double photoionization of a target atom by one photon is described by treating the absorbed radiation as a perturbation, yielding the so-called first-order driven Schrödinger equation (in atomic units, here used throughout),

$$(E_0 + \omega - H)|\Psi_{sc}^+\rangle = \boldsymbol{\epsilon} \cdot \boldsymbol{\mu}|\Psi_0\rangle = \left(\frac{d}{dz_1} + \frac{d}{dz_2}\right)|\Psi_0\rangle, \tag{2}$$

where Ψ_{sc}^+ is the purely outgoing wave function which includes double photoionization, Ψ_0 is the initial bound state of the target H^- atom with energy E_0, $\boldsymbol{\epsilon}$ is the polarization direction of the photon defining the z axis of the laboratory

frame, and $\boldsymbol{\mu}$ is the dipole operator, shown in Eq. (2) in the velocity gauge. With this choice of orientation, the final state for one-photon absorption from a ^1S atom has the symmetry $^1P_0$. Thus, the selection rules associated with a dipole-allowed transition significantly reduce the number of angular momentum channels that must be considered, restricting the final state to include only $L=1, M=0$ contributions.

The atomic double-photoionization amplitude $f(\mathbf{k}_1,\mathbf{k}_2)$ associated with Ψ_{sc}^+ in an ECS approach has been shown to be given, up to an irrelevant overall phase, by an integral over a finite volume within R_0 [50,51],

$$f(\mathbf{k}_1,\mathbf{k}_2) = \langle \Phi_Z^{(-)}(\mathbf{k}_1,\mathbf{r}_1)\Phi_Z^{(-)}(\mathbf{k}_2,\mathbf{r}_2)|E-T-V_1|\Psi_{sc}^+\rangle, \quad (3)$$

where E is the total energy, T is the two-electron kinetic energy operator, and V_1 is the sum of all atomic nuclear attraction potentials,

$$V_1 = -Z/r_1 - Z/r_2. \quad (4)$$

The distorted wave "testing functions" $\Phi_Z^{(-)}(\mathbf{k}_1,\mathbf{r}_1)$ in Eq. (3) are momentum-normalized atomic Coulomb functions with charges Z equal to the charge of the nuclear potential in V_1 of Eq. (4), which is $Z=1$ in the case of H^-. With that choice of effective nuclear charge on the testing functions, the finite-volume amplitude integral above projects out single-ionization contamination from the double-ionization channel by orthogonality of the Coulomb functions to the residual bound one-electron atom [35]. This choice for Z is in contrast to the usual "Peterkop condition" [33],

$$\frac{Z}{k_1}+\frac{Z}{k_2} = \frac{1}{k_1}+\frac{1}{k_2}-\frac{1}{\mathbf{k}_1-\mathbf{k}_2}, \quad (5)$$

which is formally adopted to eliminate an overall volume-dependent phase. This phase, however, has been shown to have no effect on the calculated cross sections [52]. It must be stressed that the final state in Eq. (3) is not given by a product of Coulomb functions but is contained in the outgoing wave Ψ_{sc}^+; the Coulomb functions serve to extract the double-ionization amplitude from all other energetically allowed processes (e.g., single-ionization channels) contained in the exact solution.

The six-dimensional finite-volume integral of Eq. (3) also leads to a further computational simplification by application of Green's theorem, thus allowing the amplitude to be computed as a surface integral. This allows the amplitude to be evaluated by considering only the asymptotic form of the scattered wave. The five-dimensional surface integral evaluated in hyperspherical coordinates is given by

$$f(\mathbf{k}_1,\mathbf{k}_2) = \int d\Omega_1 \int d\Omega_2 \int d\rho \int_0^{\pi/2} d\alpha \frac{\rho^5 \sin^2\alpha \cos^2\alpha}{2} \times \Phi_Z^{(-)}(\mathbf{k}_1,\mathbf{r}_1)^* \Phi_Z^{(-)}(\mathbf{k}_2,\mathbf{r}_2)^* \times \left(\frac{\overleftarrow{\partial}}{\partial\rho}\delta(\rho-\rho_0) - \delta(\rho-\rho_0)\frac{\overrightarrow{\partial}}{\partial\rho} \right) \Psi_{sc}^+(\mathbf{r}_1,\mathbf{r}_2), \quad (6)$$

where the arrows above the partial derivatives indicate the direction in which they operate and the δ functions enforce the evaluation of the amplitude along the hypersphere defined by $\rho=\sqrt{r_1^2+r_2^2}$. The hyperangle α is defined by $\tan\alpha = r_2/r_1$, while Ω_1 and Ω_2 are the spherical polar angular coordinates of electrons 1 and 2, respectively.

The triply differential cross section describing the angular distributions of both ejected electrons and the energy sharing between them is given by

$$\frac{d^3\sigma}{dE_1 d\Omega_1 d\Omega_2} = \frac{4\pi^2}{\omega c} k_1 k_2 |f(\mathbf{k}_1,\mathbf{k}_2)|^2. \quad (7)$$

C. Partial wave decomposition of Ψ_{sc}^+ and the double-photoionization amplitude

Following the prescription for practical calculation of the double-photoionization amplitude utilized for both atomic helium [25] and molecular hydrogen [29], we seek to decompose the full scattered wave into angular components on a radial grid in order to implement exterior complex scaling. Thus, the scattered wave function that solves Eq. (2) is expanded as

$$\Psi_{sc}^+ = \sum_{l_1 m_1} \sum_{l_2 m_2} \frac{1}{r_1 r_2} \psi_{l_1 m_1, l_2 m_2}(r_1,r_2) Y_{l_1 m_1}(\hat{\mathbf{r}}_1) Y_{l_2 m_2}(\hat{\mathbf{r}}_2), \quad (8)$$

where, unlike our earlier helium treatment, we have not explicitly partitioned the sum into direct and exchange components, but have instead summed over angular configurations (i.e., lm pairs) of the individual electrons. This sum, of course, is over lm-pair configurations that give an overall $L=1$, $M=0$ state required by photoabsorption selection rules. The two-dimensional radial function $\psi_{l_1 m_1, l_2 m_2}(r_1,r_2)$ multiplying the product of spherical harmonics is represented in a product basis of one-dimensional (1D) finite-element-method (FEM) discrete-variable representation (DVR) functions, similar to the approach used in molecular hydrogen DPI referenced above. For overall singlet symmetry, the radial functions, under exchange of the coordinates of the two electrons, have the property

$$\psi_{l_1 m_1, l_2 m_2}(r_1,r_2) = \psi_{l_2 m_2, l_1 m_1}(r_2,r_1). \quad (9)$$

The FEM DVR radial basis is an attractive choice because of the computational efficiency gained as well as the natural complementarity for implementing exterior complex scaling [49].

The Coulomb functions in Eq. (3) are similarly expanded in partial waves,

$$\Phi_Z^{(-)}(\mathbf{k},\mathbf{r}) = \left(\frac{2}{\pi}\right)^{1/2} \sum_{l,m} \frac{i^l e^{-i\eta_l}}{kr} \phi_{l,k}^{(c)}(r) Y_{lm}(\hat{\mathbf{r}}) Y_{lm}^*(\hat{\mathbf{k}}), \quad (10)$$

where $\phi_{l,k}^{(c)}(r)$ is a radial Coulomb function with asymptotic form

$$\phi_{l,k}^{(c)}(r) \to \sin[kr + (Z/k)\ln 2kr - l\pi/2 + \eta_l(k)] \quad (11)$$

as $r\to\infty$, and η_l represents the Coulomb phase

$$\eta_l(k) = \arg\Gamma(l+1-iZ/k), \quad (12)$$

with Z equal to the nuclear charge in the one-body potentials of Eq. (4). Here $Z=1$ for H^-.

By substituting the partial wave expansions of the full scattered solution Ψ_{sc}^{+} [Eq. (8)] and the product of testing functions $\Phi_Z^{(-)}(\mathbf{k},\mathbf{r})$ [Eq. (10)] into the expression for the full amplitude [Eq. (6)] and integrating over the angular coordinates $d\Omega_1 d\Omega_2$ of both electrons, we arrive at an expression connecting the partial waves of Ψ_{sc}^{+} with the product of Coulomb waves,

$$f(\mathbf{k}_1,\mathbf{k}_2) = \sum_{l_1,m_1}\sum_{l_2,m_2}\left(\frac{2}{\pi}\right) i^{-(l_1+l_2)} e^{i\eta_{l_1}(k_1)+i\eta_{l_2}(k_2)} \times [\mathcal{F}_{l_1,l_2,m_1,m_2}(k_1,k_2) Y_{l_1 m_1}(\hat{\mathbf{k}}_1) Y_{l_2 m_2}(\hat{\mathbf{k}}_2)], \tag{13}$$

due to the orthogonality of the spherical harmonics. The sum is once again constrained to include only angular momentum pairs for which $M=m_1+m_2=0$. Using the standard theory of rearrangement scattering, combined with a two-potential formalism, we can express the partial wave amplitudes $\mathcal{F}_{l_1,l_2,m_1,m_2}(k_1,k_2)$ appearing in Eq. (13) as [35]

$$\begin{aligned}\mathcal{F}_{l_1,l_2,m_1,m_2}(k_1,k_2) &= \frac{1}{k_1 k_2} \times \langle \phi_{l_1,k_1}^{(c)}(r_1)\phi_{l_2,k_2}^{(c)}(r_2)|E-h_1 \\ &\quad -h_2|\psi_{l_1 m_1,l_2 m_2}(r_1,r_2)\rangle \\ &= \frac{1}{k_1 k_2}\int dr_1 dr_2 \phi_{l_1,k_1}^{(c)}(r_1)\phi_{l_2,k_2}^{(c)}(r_2) \\ &\quad \times (E-h_1-h_2)\psi_{l_1 m_1,l_2 m_2}(r_1,r_2),\end{aligned} \tag{14}$$

where h_1 and h_2 are one-electron radial Hamiltonians,

$$h_i = -\frac{1}{2}\frac{d^2}{dr_i^2} + \frac{l(l+1)}{2r_i^2} - \frac{Z}{r_i}. \tag{15}$$

As before, the radial volume integral can be simplified by application of Green's theorem,

$$\begin{aligned}&\langle \phi_{l_1,k_1}^{(c)}(r_1)\phi_{l_2,k_2}^{(c)}(r_2)|E-h_1-h_2|\psi_{l_1 m_1,l_2 m_2}(r_1,r_2)\rangle \\ &= \frac{\rho_0}{2}\int_0^{\pi/2}\left(\phi_{l_1,k_1}^{(c)}(r_1)\phi_{l_2,k_2}^{(c)}(r_2)\frac{\partial}{\partial\rho}\psi_{l_1 m_1,l_2 m_2}(r_1,r_2)\right. \\ &\quad \left. -\psi_{l_1 m_1,l_2 m_2}(r_1,r_2)\frac{\partial}{\partial\rho}\phi_{l_1,k_1}^{(c)}(r_1)\phi_{l_2,k_2}^{(c)}(r_2)\right)\Bigg|_{\rho=\rho_0} d\alpha,\end{aligned} \tag{16}$$

where ρ_0 defines the hypersphere where the partial wave amplitudes are calculated, usually just inside the ECS turning point R_0.

D. Cross section evaluation from reduced amplitudes

The partial wave amplitudes evaluated using Eqs. (14) and (16) are then returned to Eq. (13) to construct the full double-photoionization amplitude $f(\mathbf{k}_1,\mathbf{k}_2)$. The TDCS can then be calculated by Eq. (7).

The singly differential cross section (SDCS), describing the energy sharing between the two ejected electrons, is given by integrating the TDCS over all angles $d\Omega_1 d\Omega_2$ of electrons 1 and 2. Because of the orthonormality of the spherical harmonics, cross terms between reduced amplitudes for different angular configurations disappear; thus the SDCS is simply given by

$$\frac{d\sigma}{dE_1} = \frac{4\pi^2}{\omega c}k_1 k_2\left(\frac{2}{\pi}\right)^2 \sum_{l_1 m_1}\sum_{l_2 m_2}|\mathcal{F}_{l_1,l_2,m_1,m_2}(k_1,k_2)|^2. \tag{17}$$

The total cross section for double photoionization is then given by integrating the SDCS over the energy sharing range,

$$\sigma = \int_0^E \frac{d\sigma}{dE_1}dE_1, \tag{18}$$

although the SDCS is sometimes defined to give the total cross section by integration over half the energy range. Because the SDCS is symmetric about $E/2$, this simply redefines the SDCS as

$$\frac{d\tilde{\sigma}}{dE_1} = 2\frac{d\sigma}{dE_1}, \tag{19}$$

thus also making the total DPI cross section

$$\sigma = \int_0^{E/2}\frac{d\tilde{\sigma}}{dE_1}dE_1. \tag{20}$$

For consistency with our published SDCS results for helium, we have adopted the convention of Eq. (20) in this work.

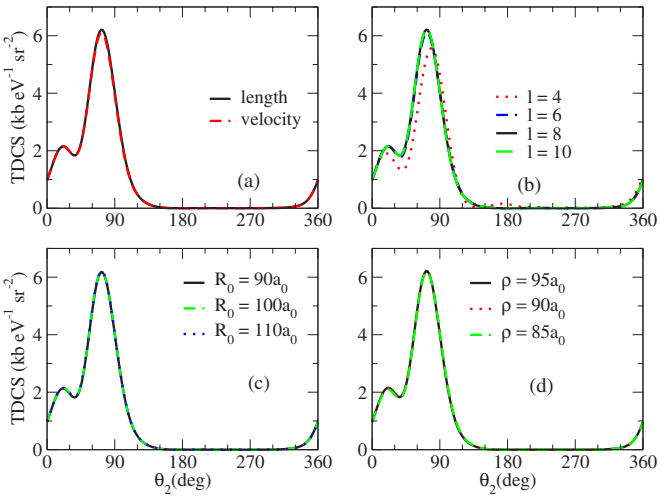

FIG. 2. (Color online) Convergence tests for the H^- TDCS, calculated at 18 eV photon energy with the first electron direction fixed at $\theta_1=40°$ and carrying 80% of the excess energy. (a) TDCS results calculated in both length and velocity gauges. (b) Convergence of velocity-gauge results as more partial wave terms are included. (c) Convergence with respect to the radial grid, varying the extent of the complex scaling point R_0. (d) Convergence of the TDCS with different hyperspherical radii ρ for evaluation of the finite-volume amplitude calculations. Cross sections in units of kilobarns (kb) per eV per steradian (sr). 1 kb$=10^{-21}$ cm^2. R_0 in units of a_0. $1a_0=0.529\times10^{-8}$ cm.

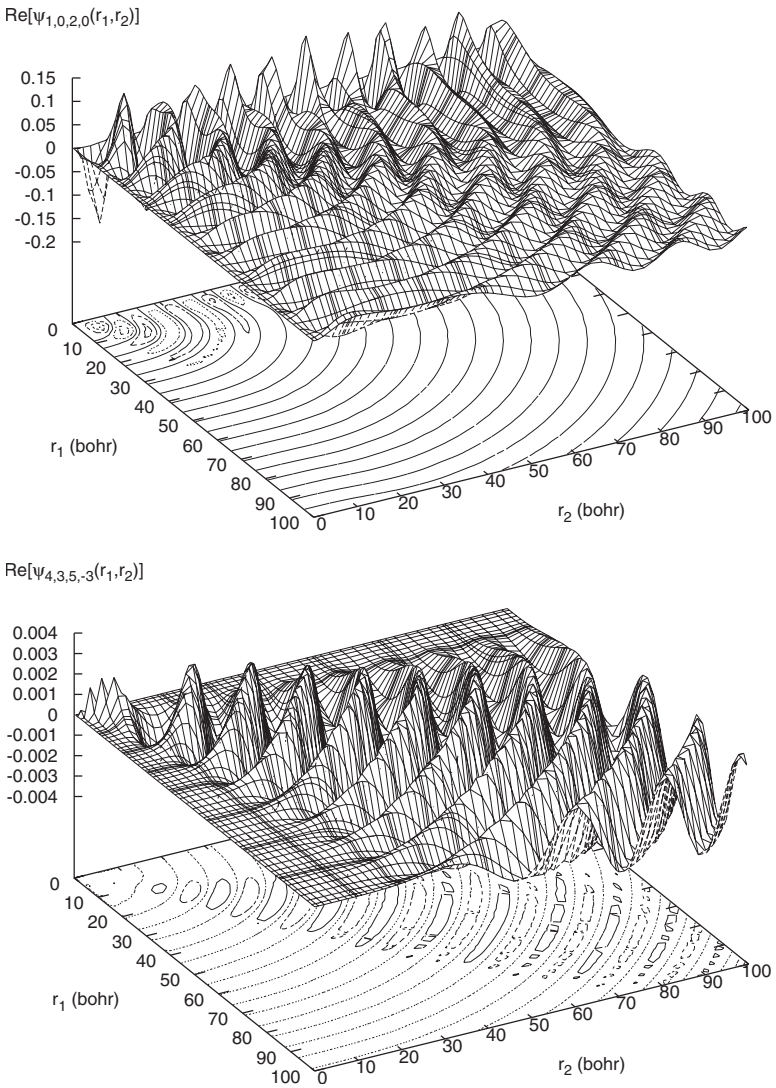

FIG. 3. Real component of two partial waves, labeled by the angular momentum of each electron (l_1,m_1,l_2,m_2), contributing to the full scattered wave function. The upper panel corresponds to the angular contribution $(1,0,2,0)$. The lower panel shows the partial wave for $(4,3,5,-3)$. Peaks along the r_1 or r_2 axis correspond to amplitude in single-ionization channels. r_1 are r_2 and in units of bohr. 1 bohr$=0.529\times10^{-8}$ cm.

III. CALCULATED CROSS SECTIONS FOR DOUBLE PHOTOIONIZATION OF H^-

In order to solve the driven Schrödinger equation [Eq. (2)] for the scattered wave, we must first describe the fully correlated ground state Ψ_0 in our FEM DVR basis. This was accomplished by solving for the lowest eigenstate of the H^- Hamiltonian described on a grid with 15 Lobatto quadrature points within each of three finite elements chosen at $r=5.0a_0$, $r=10.0a_0$, and $r=20.0a_0$. Such a large radial grid is required to describe the especially long exponential tail of the H^- ground-state wave function. In addition, up to $l=4$ was used to describe the ^1S state, yielding a ground state energy of −0.527 68 hartrees. The exact ground-state energy of H^- is −0.527 75 a.u. [53], indicating that electron correlation is well accounted for in our ground-state wave-function expansion.

A. Convergence tests

The final-state ^1P continuum of Ψ_{sc}^+ from which the following cross sections were calculated was expanded according to Eq. (8) on a radial grid with 15th-order DVR points in several finite elements with an ECS turning point at $R_0=100$ bohrs. This large grid size is more consistent with those used in atomic hydrogen electron-impact ionization problems. It follows that a larger grid is required to fully capture the dynamics involved in DPI when the nuclear attraction potential diminishes in magnitude in going from $Z=2$ to $Z=1$. This observation was discussed in the B-spline treatment of DPI from helium [25] and in the FEM DVR calculation of molecular hydrogen DPI [29], where smaller radial grids were sufficient to produce converged results.

Figure 2 demonstrates the convergence of the calculated results with respect to several parameters. The triply differential cross sections were calculated for an 18 eV photon with the fixed electron leaving at an angle $\theta_1=40°$ and with 80% of the available excess energy. Unless otherwise stated, the TDCSs are plotted for "coplanar geometry," where the polarization vector and the photoelectron momenta all lie in the same plane. A comparison of the cross sections calculated in the length and velocity gauges is shown in Fig. 2(a). The differences between calculations taken in the length and velocity gauges are graphically indistinguishable in these TDCS plots. Therefore the other TDCS results in Fig. 2 and

in the examples throughout this work, unless otherwise stated, are shown only in the velocity gauge.

Figure 2(b) demonstrates the convergence of the calculated results with increasing numbers of partial waves. The results shown were computed using a value of $l=4$ for the initial state Ψ_0 and the various maximum l values shown to describe the final state Ψ_{sc}^{+}. Increasing the number of partial waves in the initial state to $l=5$ showed no changes from these results, indicating an accurate description of the ground state wave function was used. The general trend of the TDCSs is given by the $l=4$ results, with the most significant change occurring by including up to $l=6$ partial waves. The results for maximum $l=8$ and 10 are nearly identical, indicating that inclusion of partial waves of up to $l=8$ yields converged results.

It should be noted that the number of partial waves necessary to give converged results for H^- is significantly larger than the maximum value of l used to treat double photoionization in helium [25]. The electron-electron repulsion term $1/|r_1-r_2|$, which is treated by a multipole expansion, is more dominant for H^- than for any other two-electron atom. Thus, the accuracy of the computed results depends more sensitively on the number of partial waves taken for H^- compared to helium, requiring higher-l terms to converge the calculation as electron repulsion becomes more significant.

In addition to the angular decomposition, converged results must be robust with respect to the radial component parameters. The variation of the computed TDCS with radial grid extent is shown in Fig. 2(c). The exterior complex scaling point R_0 was placed at 90, 100, and 110 bohrs. The results are insensitive to this change, further indicating that our radial basis is essentially complete and that the calculation is converged.

Finally, to ensure that the radial grid is sufficient to extract accurate double-photoionization amplitudes by means of the finite volume integral of Eq. (3), Fig. 2(d) shows TDCS results calculated at different extraction radii ρ just before the ECS turning point $R_0=100a_0$. The physically meaningful DPI amplitude should be insensitive to the finite volume used to extract it from the outgoing scattered wave, provided that such a finite volume is large enough to fully account for the dynamics of the problem. Figure 2(d) illustrates that that is the case.

With these issues of convergence now resolved, we now examine the components of the outgoing scattered wave that make up the full solution. Such an exercise reveals interesting aspects about the partial wave contributions to double photoionization as well as the competing single photoejection process. Figure 3 displays the real part of two contributing partial waves of the full solution Ψ_{sc}^{+} along the real radial grid. The upper panel shows $\mathrm{Re}(\psi_{l_1m_1,l_2m_2})$ for a low-angular-momentum pair $l_1=1, m_1=0, l_2=2, m_2=0$. The contributions of this partial wave to single ionization are evidenced by the large peaks near the r_2 axis where r_1 is small. The relative magnitude of the higher-angular-momentum partial wave shown in the lower panel is much smaller, but displays a significant contribution to the double-photoionization channel. By contrast, the relative contribution of this higher-angular-momentum component to single ionization or excitation ionization is evidently very small.

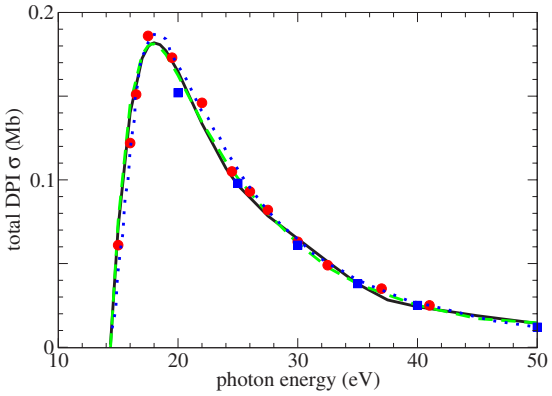

FIG. 4. (Color online) Total double-photoionization cross section of H^- at various energies. The solid and dashed curves correspond to the present results calculated in the length and velocity gauges, respectively. Circles correspond to results calculated through wave-packet propagation by Foumouo *et al.* [45]. Squares correspond to results reported by Pindzola and Robicheaux calculated using TDCC methods [44]. Dotted curve corresponds to results in the velocity gauge reported by Kheifets and Bray calculated using CCC methods [43]. Cross sections in units of megabars (Mb). 1 Mb$=10^{-18}$ cm^2.

The significance of the high-partial-wave components confirms the importance of electron correlation in describing the double-photoionization process.

B. Total double-photoionization cross section

Previously published theoretical calculations treating double photoionization of H^- have only presented total DPI cross sections. To compare with some of these results, we calculated the total DPI cross section at several energies according to Eq. (20). The results are presented in Fig. 4. The results calculated in both the length and velocity gauges are nearly identical and agree well with the results calculated by wave-packet propagation [45], by time-dependent close coupling [44], and by convergent close coupling in the velocity gauge [43] (circles, squares, and diamonds in Fig. 4, respec-

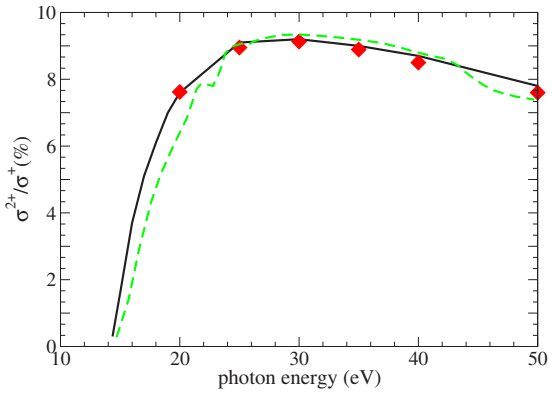

FIG. 5. (Color online) Ratio of double to single ionization cross sections of H^- as a function of photon energy. Solid curve, present results calculated in the velocity gauge; broken curve, results of Ref. [42]; diamonds, results of Ref. [44].

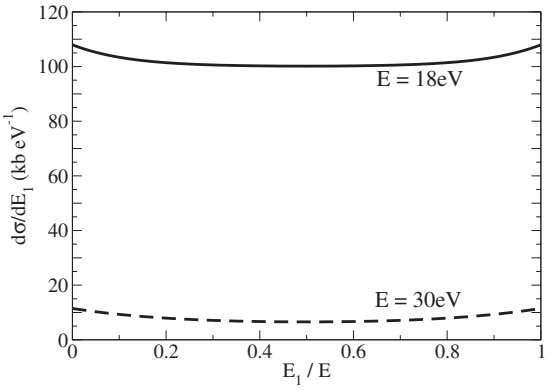

FIG. 6. Single differential cross section for DPI of H^- at two photon energies 18 (solid curve) and 30 eV (dashed curve), plotted as a function of the fractional energy carried by one electron. The product of half the area under each curve and the excess energy above the double-ionization threshold yields the integral DPI cross section.

tively). In addition, we calculated the ratio of single to double photoionization; the results are shown in Fig. 5. The single-ionization cross sections were obtained by subtracting the calculated total DPI cross section from the total photoabsorbtion cross section obtained from the optical theorem. Our calculated single to double photoionization ratios are in good agreement with the velocity gauge results of Kheifets and Bray [43] (not shown) and Pindzola and Robicheaux [44]. Below 25 eV, they are somewhat higher than the results of Meyer *et al.* [42].

Some interesting things to note about the DPI cross section of H^- include its rather large magnitude compared to that of helium, consistent with its small, correlation-induced binding energy. The double to single photoionization cross section ratio peaks at ~3.7% for helium, while for H^- the peak ratio is substantially larger, near 10%. In addition, the location of the maximum for H^- is only a few eV above its threshold, whereas the maximum total cross section for helium lies ~20 eV above the DPI threshold. However, the ratios of excess energy to the double-ionization potential at these maxima are nearly the same.

C. Single differential cross sections at 18 and 30 eV

The single differential cross section results for photon energies 18 and 30 eV are shown in Fig. 6. At ω=18 eV, representing the maximum integral DPI cross section, the SDCS for H^- is two orders of magnitude larger than the size of the largest SDCS for helium, and quickly diminishes in magnitude as the photon energy is increased. The general variation of the SDCS as the energy shared between the electrons changes, however, appears like those exhibited in helium and molecular hydrogen. In all these cases, the SDCSs feature a similar trend as shown in Fig. 6, with a relatively flat curve that increases by only a few percent as the energy sharing becomes more unequal.

D. Triple differential cross sections at 18 and 30 eV

The most detailed information that can be observed in a double-photoionization experiment is the triple differential cross section. We begin by considering the variation of the cross section with energy sharing. Figure 7 shows computed TDCS results for an 18 eV photon (3.64 eV above threshold) with θ_1=0°, i.e., with the first electron ejected along the polarization axis. The panels feature cases of energy sharings, from top to bottom, of 15%, 35%, 50%, 65%, and 85% for the first electron. Included in Fig. 7 are the corresponding TDCS results for DPI of helium calculated at peak energy (20 eV above threshold). The magnitude of helium cross sections has been scaled by a factor of 100. As the energy sharing is varied from the equal-sharing case, the cross section increases toward the direction opposite the first electron, similar to the case for helium. However, the H^- case shows a much more rapid approach to the opposite direction of ejection at less unequal energy sharings than does helium. The general shape of TDCS for helium at 15% and 85% energy sharing thus agree more with the TDCS corresponding to

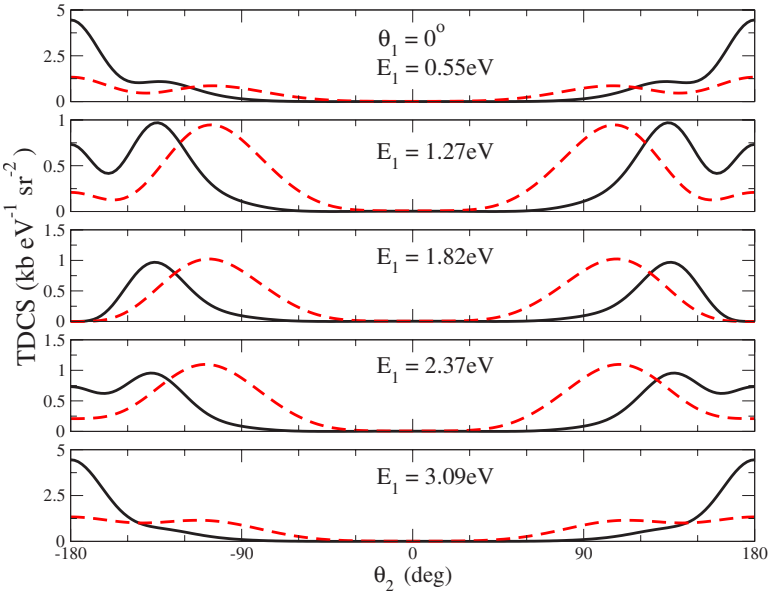

FIG. 7. (Color online) TDCS for double photoionization of H^- with a photon 3.64 eV above threshold (solid line) and of helium with a photon 20 eV above threshold (dashed line), with θ_1 fixed at 0°, at various energy sharings. The energy of the fixed electron (E_1) corresponds to energy sharings of 15%, 35%, 50%, 65%, and 85%, top to bottom panels, respectively. Selection rules [13] prevent the second electron from exiting opposite the first in the center panel. As the symmetry is broken, this quickly becomes the preferred direction. The results for helium are scaled by a factor of 100.

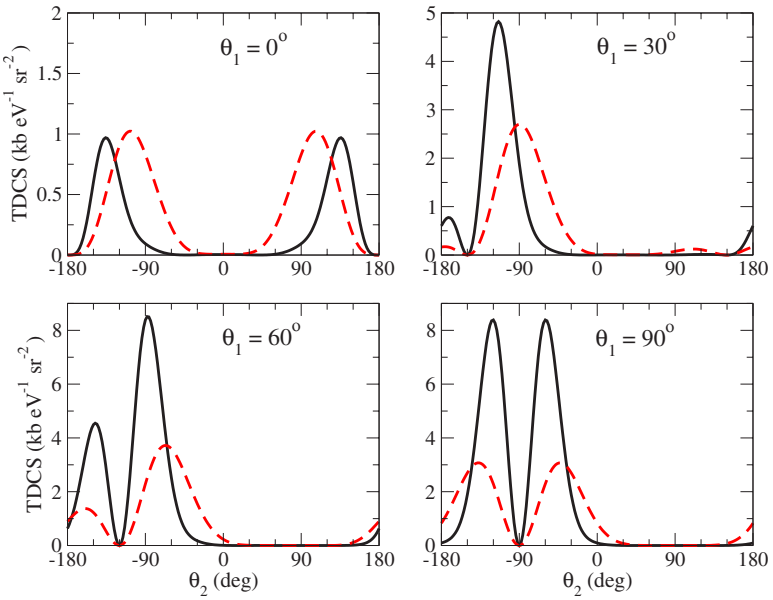

FIG. 8. (Color online) TDCS of H^- for a photon 3.64 eV above threshold (solid curve) with various fixed first electron angles θ_1 and equal energy sharing. The dashed curves are similar cases involving DPI of helium at 20 eV above threshold, scaled by a factor of 100. Selection rules cause the cross section to disappear opposite θ_1.

35%and 65% energy sharings, respectively, in the case of H^-. In addition, the more extreme unequal-energy-sharing cases for H^- show a larger variation in the magnitude of the cross sections relative to equal energy sharing than does the helium case.

Figure 8 shows H^- TDCS results for various equal-energy-sharing orientations at 18 eV photon energy. In general, the peaks are narrower for H^- when compared to similar cases of DPI of helium at 20 eV above threshold, also shown in Fig. 8, but the overall trends within each panel and variation as the orientation of the first outgoing electron changes are similar to those of helium. The locations of the peaks in θ_2 are slightly further away from the fixed ejected electron's direction in H^- compared to the corresponding peak angles found in helium. This seems reasonable given the more significant contribution of electron repulsion in H^- than in helium. Again, the magnitude of the TDCS variation changes more dramatically for H^- than for helium as the first electron orientation is varied. The TDCS relative magnitude changes are two to three times larger in H^- than the variations observed for helium. Similarly evident from the panels in Fig. 8, as in the helium case, is the selection rule that prevents the two electrons from exiting in opposite directions at equal energy sharing [13].

Figure 9 displays TDCS results for a fixed electron at $\theta_1 = 30°$ at various energy sharings for both H^- and helium at peak double-photoionization energies. Again, similar trends exist between these examples for H^- and helium as the energy sharing is varied, the most pronounced differences between the two cases occurring when one electron moves

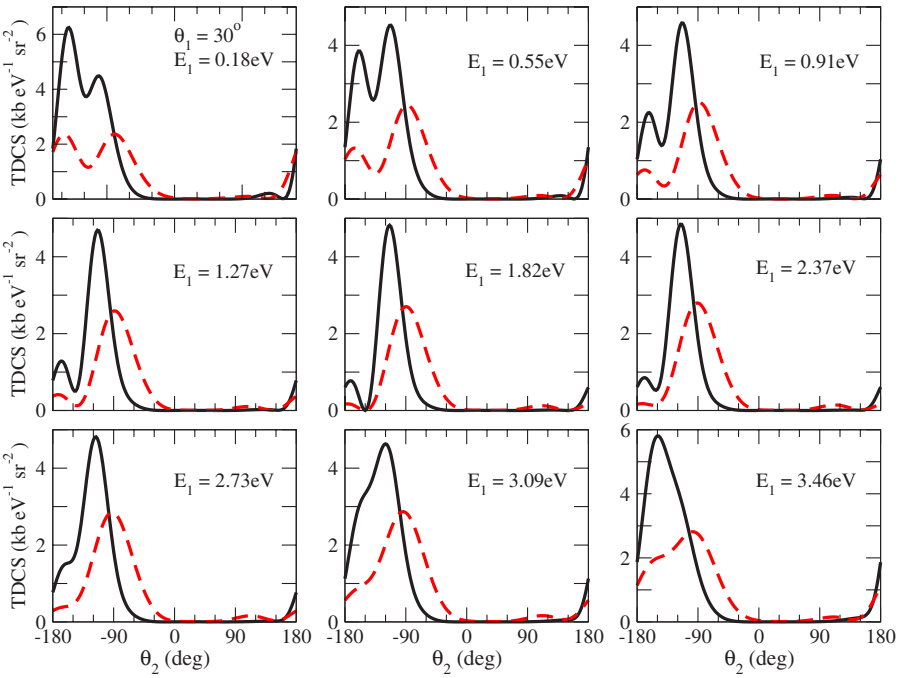

FIG. 9. (Color online) H^- double-photoionization TDCS for a photon 3.64 eV above threshold (solid curve) with fixed first electron angle $\theta_1 = 30°$ at various energy sharings. Also shown are corresponding TDCS results for DPI of helium at 20 eV above threshold (dashed curve) scaled by a factor of 100. The panels correspond to 5%, 15%, 25%, 35%, 50%, 65%, 75%, 85%, and 95% available energy carried by the first electron.

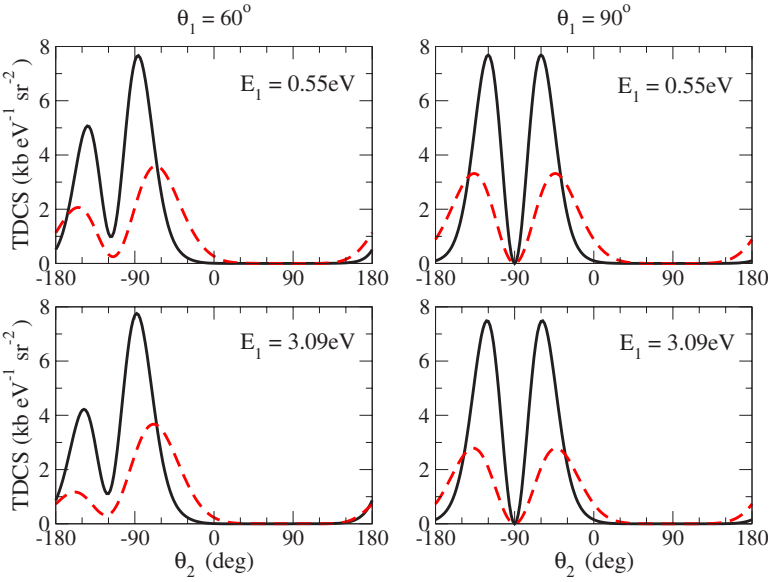

FIG. 10. (Color online) TDCS of double photoionization of H^- for a photon 3.64 eV above threshold (solid curve) and helium for a photon 20 eV above threshold (dashed curve) with fixed first electron angles $\theta_1=60°$ (first column) and 90° (second column) and at energy sharings of 15% (first row) and 85% (second row) available energy carried by the first electron. The helium results have been scaled by a factor of 100.

away much faster than the other. The angles of the maximum cross section for H^- again vary further away from the first electron compared to helium as mentioned above.

The TDCS results for different orientations ($\theta_1=60°$ and 90°) with unequal energy sharing ($E_1=15\%$ and 85% of 3.64 eV above threshold) are shown in Fig. 10. The general features of the cross sections appear similar to the corresponding cases for helium DPI at peak photon energy, shown as the dashed line in Fig. 10.

To better visualize the double ionization beyond the coplanar geometry, i.e., with both electrons exiting in the same plane as the polarization, three-dimensional TDCS results of DPI from H^- at 3.64 eV above threshold are shown in the upper panel of Fig. 11. The lower panel displays a corresponding TDCS calculated for helium DPI by a photon with 20 eV above threshold energy. The first electron in both cases is fixed at $\theta_1=30°$ with equal energy sharing. Again, the selection rule preventing the second electron from being ejected opposite θ_1 is demonstrated, causing a flattening out of the larger lobe near $\theta_2=210°$. More prominent than in the helium case is the small lobe near $\theta_2=180°$. The case of unequal energy sharing is illustrated in the two panels of Fig. 12, where the upper panel displays the H^- three-dimensional TDCS with the first electron carrying away 15% of the available energy and the lower panel displays similar results calculated for helium. The nonapplicability of the equal-energy-sharing selection rule is most apparent for both cases. The lengths of the arrows for the H^- results shown in the upper panels of Figs. 11 and 12 correspond to 1600 b eV^{-1} sr^{-1}, while for the helium cases of the lower panels the arrow lengths correspond to 20 b eV^{-1} sr^{-1}. The H^- cross sections of Figs. 11 and 12 exhibit a magnitude several orders larger than for helium, but perhaps most striking is the orientation of the larger lobe away from the *xy* plane for H^-. The helium case shows a preferred ejection into the *xy* plane away from the first electron. The different orientation of the major lobes for H^- and helium is illustrated more dramatically in three dimensions.

One of the influences on the features of the triple differential cross sections is the energy above threshold available

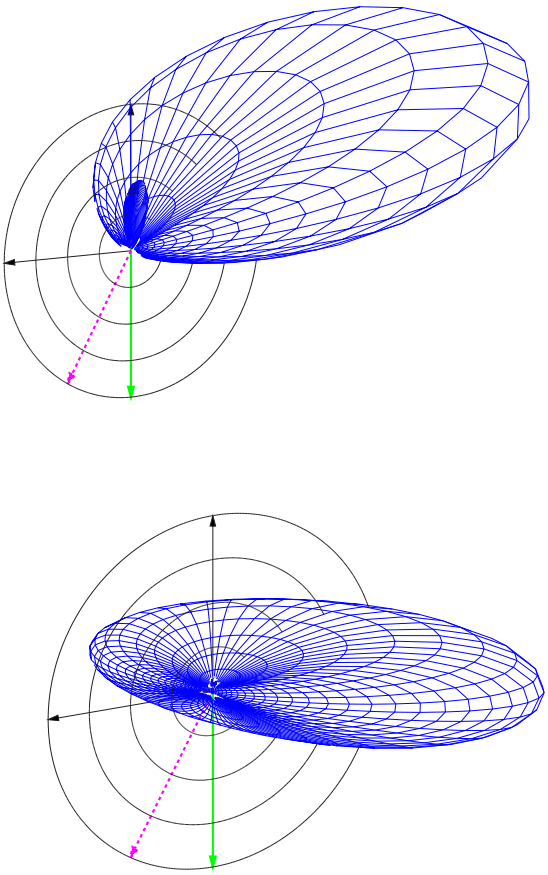

FIG. 11. (Color online) Three-dimensional TDCS results for DPI of H^- with a photon 3.64 eV above threshold (upper panel) and for helium with a photon 20 eV above threshold (lower panel) with equal energy sharing and the first electron ejected in a direction fixed at $\theta_1=30°$ (shown as dashed arrow) from the polarization direction (solid arrow). The direction of the larger lobe is further away from the fixed direction θ_1 in H^- than is observed for helium. The arrow lengths of the H^- panel are 80 times larger than those shown in the lower panel for helium.

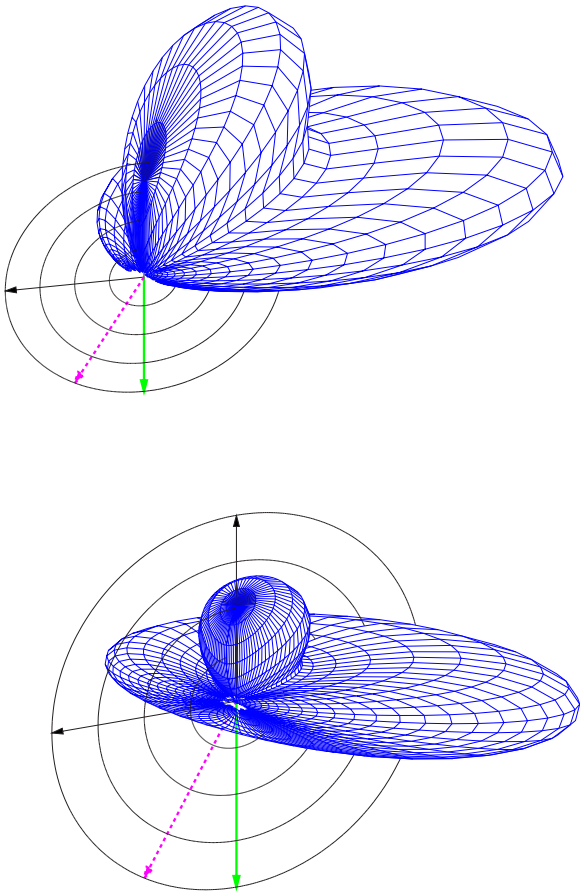

FIG. 12. (Color online) Three-dimensional TDCS results for DPI of H^- involving a photon 3.64 eV above threshold (upper panel) and for helium with a photon 20 eV above threshold (lower panel) with 15% energy sharing carried by the first electron into the fixed direction $\theta_1=30^\circ$ (shown as dashed arrow) from the polarization direction (solid arrow). The breakdown of the selection rule manifest in Fig. 11 is apparent. The arrow lengths of the H^- panel are 80 times larger than those shown in the lower panel for helium.

to both electrons. Foster and Colgan [54] report calculated TDCS results that show comparable angular features for cases in which the ratio of excess energy available to the ejected electrons to the corresponding double-ionization potential is similar for two-electron atoms with $Z \geq 2$. The cross sections calculated above for H^- have been calculated at an energy where the total DPI cross section is maximal, lying at an energy close to the double-ionization threshold. Because the general features may be strongly influenced by threshold effects, we now consider the TDCS results calculated for double photoionization with a photon of 30 eV, 15.64 eV above the H^- double-ionization threshold. This photon energy corresponds to total ejection energies closer to those for which TDCS results for helium have been measured experimentally and theoretically calculated.

Figure 13 shows TDCSs calculated for H^- at 30 eV photon energy with equal energy sharing at various ejected electron angles. Comparing these results and those calculated for H^- at 18 eV (Fig. 8) with results calculated at 20 eV above threshold for helium (shown as the dashed line in Fig. 13) demonstrates that there are more similarities between H^- and helium at more comparable above-threshold energies for equal energy sharing. The results of Fig. 13 demonstrate that the cross section peaks as a function of θ_2 at angles more similar to helium at this higher photon energy. Furthermore, the relative magnitude of the cross section features both within each panel and among the different angles for θ_1 are closer to those exhibited in helium than the nearer-to-threshold case shown in Fig. 8.

The case of unequal energy sharing at 30 eV photon energy and fixed angle for one ejected electron is illustrated in Fig. 14. The results in general show as much variation as those in Fig. 9 when compared to helium DPI at 20 eV above threshold. Consistent with the results mentioned above, better agreement between the general shape and relative peak heights compared to helium occurs for the 30 eV photon near equal energy sharing. The larger differences occur at more severe energy sharings.

Figure 15 highlights the changes that occur as the electrons have more available kinetic energy when the photon

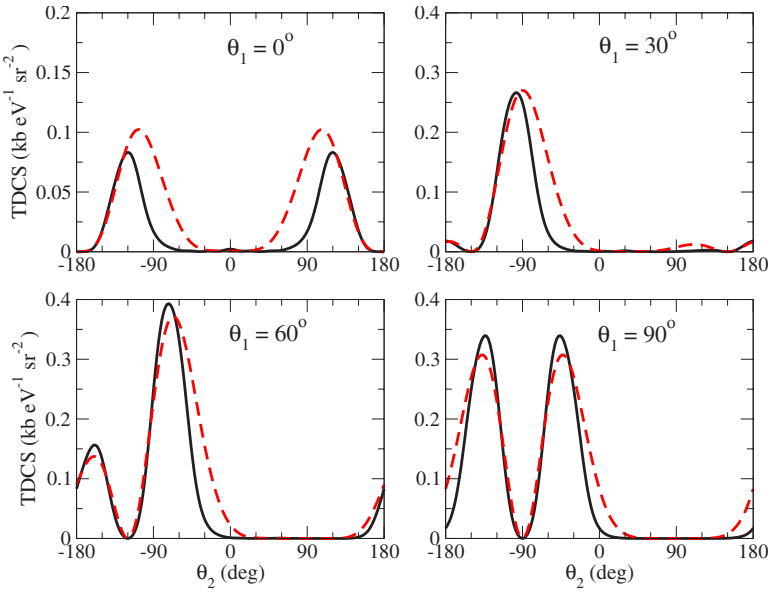

FIG. 13. (Color online) TDCS for double photoionization of H^- (solid curve) involving a 30 eV photon (15.64 eV above threshold) at various fixed first electron angles θ_1 and equal energy sharing. Also reproduced are the corresponding helium results (dashed curve) shown in Fig. 8, now scaled by a factor of 10.

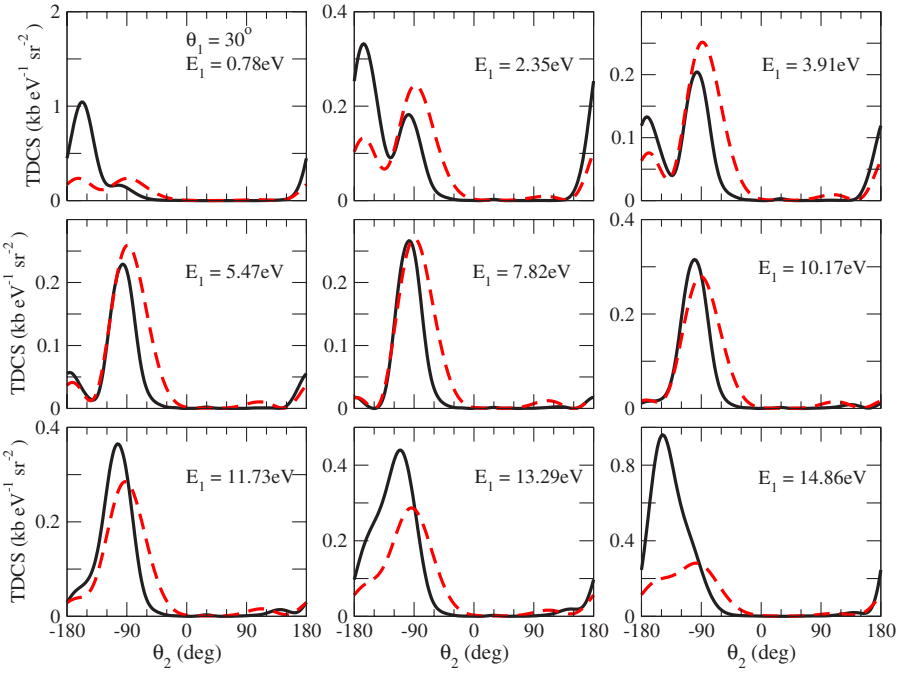

FIG. 14. (Color online) TDCS for a 30 eV photon (solid curve), 15.64 eV above the H^- DPI threshold, with fixed first electron angle $\theta_1=30°$ and various energy sharings. Also shown are the corresponding helium TDCS results displayed in Fig. 9 (dashed curve), though now scaled by a factor of 10. The panels correspond to 5%, 15%, 25%, 35%, 50%, 65%, 75%, 85%, and 95% available energy carried by the first electron.

energy is changed from 18 to 30 eV. The TDCS results calculated for various geometries and energy sharings at 30 eV scaled by a factor of 16 (solid curve) are shown along with the results calculated with an 18 eV photon from Fig. 10 (dashed curve). Also shown are the corresponding helium TDCS results calculated at photon energy 20 eV above the DPI threshold (dash-dotted curve). The overall trends are similar, but with the H^- cross section maxima located at angles closer to those in helium for the 30 eV photon.

Finally, to compare with Figs. 11 and 12 we present in Fig. 16 a three-dimensional view of the TDCS calculated at 30 eV photon energy with θ_1 fixed at 30°. The top left panel shows the case of equal energy sharing for H^-, followed by the corresponding helium case at photon energy 20 eV above threshold shown in the top right panel. The overall shape of the cross section and orientation along the *xy* plane is more similar to the results for DPI of helium than was the case for H^- shown in Fig. 11 involving an 18 eV photon. The smaller lobe opposite the larger one about the selection-rule-prohibited direction in Fig. 11 is more suppressed in the more comparable excess energy case of Fig. 16. The bottom left panel displays the case where the first electron carries away 15% of the 15.64 eV above threshold energy. In this case the cross section becomes significant in the lobe outside the *xy* plane. Here, the TDCS for H^- is significantly less like the unequal-energy-sharing case of helium, reproduced in the bottom right panel, as demonstrated in the extreme energy-sharing cases shown in Fig.14. The scale of the H^- cross sections in Fig. 16 is ten times smaller than the H^- TDCS displayed in Figs. 11 and 12.

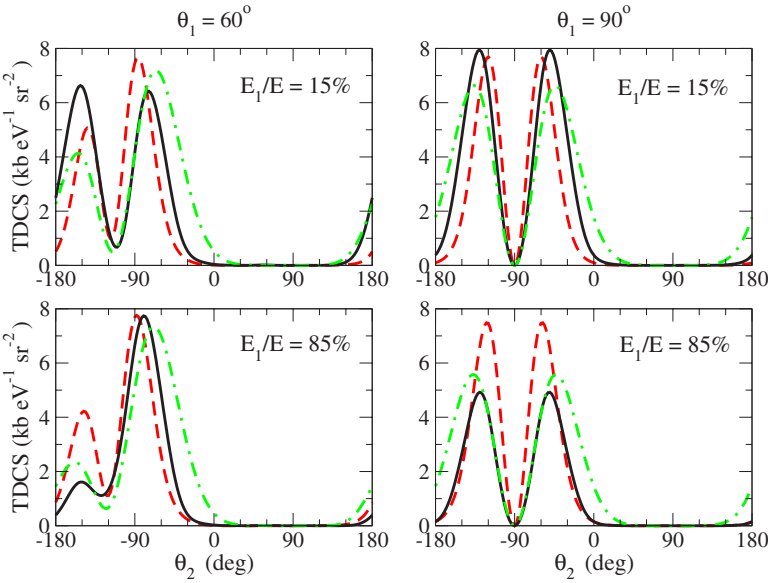

FIG. 15. (Color online) TDCS for double photoionization of H^- involving a 30 eV photon (solid curve) and an 18 eV photon (dashed curve) and for DPI of helium involving a 99eV photon (dash-dotted curve) with fixed first electron angles $\theta_1=60°$ (first column) and 90° (second column) and at energy sharings of 15% (first row) and 85% (second row) available energy carried by the first electron. The solid curve results have been scaled by a factor of 16 while the helium results have been scaled by a factor of 200.

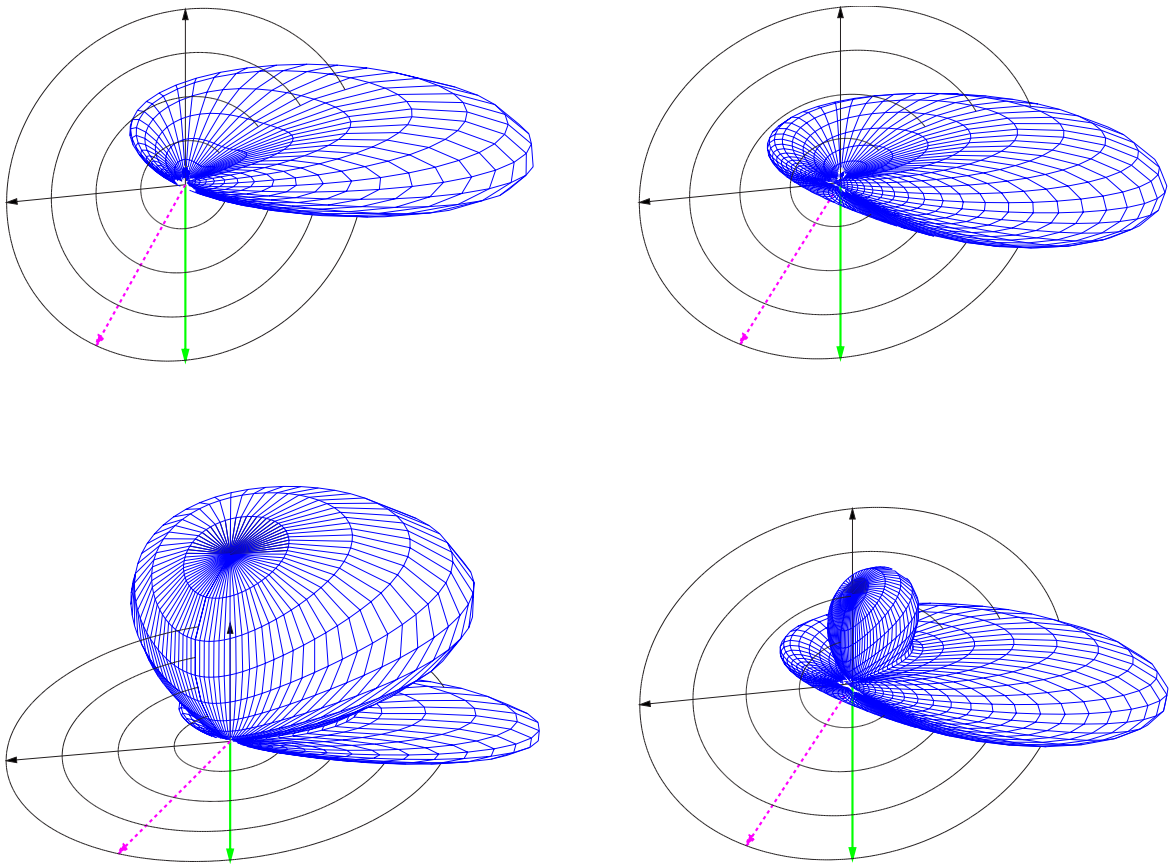

FIG. 16. (Color online) Top left panel: Three-dimensional H^- TDCS results for a 30 eV photon with equal energy sharing. Top right panel: Corresponding case for helium at 99 eV photon energy. Bottom left panel: H^- TDCS with 15% energy sharing. Bottom right panel: Unequal-energy-sharing results for helium DPI. The direction of the first ejected electron is fixed at $\theta_1 = 30°$ (shown as dashed arrow) from the polarization direction (solid arrow). The scale of the arrow lengths for the helium panels is the same as those for helium results depicted in Figs. 11 and 12, while the scale of the H^- panels is eight times greater than the helium examples depicted.

IV. CONCLUSIONS

The triple differential cross sections, representing the most detailed information measurable for atomic double-photoionization processes, have been presented for the H^- negative ion, along with SDCS and total cross section results. The H^- system presents a challenging case to treat theoretically because of the significant contribution of electron correlation to the overall dynamics, more so than for any other atomic three-body problem.

Results calculated for H^- show general trends similar to those theoretically calculated and experimentally observed in helium double photoionization, where nuclear attraction is comparatively more dominant. Significant differences between these two atomic cases however exist, most notably in the results presented at 18 eV where the total cross section is maximal. The location of this maximum near the H^- double-ionization threshold produces effects different from those observed for DPI of helium at its maximum total cross section 20 eV above threshold. When the photon energy is increased to 30 eV to provide more comparable ejection energies above threshold, the differences between the H^- and helium TDCS results appear less severe. This trend is more the case for equal energy sharing, with significant differences remaining in the extremely unequal-energy-sharing cases. These extremes with one electron moving much more slowly than the other would appear to be more sensitive to electron correlation effects in H^- than in helium, where nuclear attraction is more significant. For extreme asymmetric energy sharing, one expects postcollision interaction effects to be relatively less important, so it is not surprising that these cases reflect the significant differences in initial-state correlation between H^- and helium.

ACKNOWLEDGMENTS

This work was performed under the auspices of the U.S. Department of Energy by the University of California Lawrence Berkeley National Laboratory under Contract No. DE-AC02-05CH11231 and was supported by the U.S. DOE Office of Basic Energy Sciences, Division of Chemical Sciences.

[1] R. Wehlitz, F. Heiser, O. Hemmers, B. Langer, A. Menzel, and U. Becker, Phys. Rev. Lett. **67**, 3764 (1991).
[2] M. Braüning, R. Dörner, C. L. Cocke, M. H. Prior, B. Kriässig, A. S. Kheifets, I. Bray, A. Braüning-Demian, K. Carnes, S. Dreuil *et al.*, J. Phys. B **31**, 5149 (1998).
[3] V. Mergel, M. Achler, R. Dörner, K. Khayyat, T. Kambara, Y. Awaya, B. Nyström, L. Spielberger, J. H. McGuire, J. Feagin *et al.*, Phys. Rev. Lett. **80**, 5301 (1998).
[4] J. A. R. Samson, W. C. Stolte, Z. X. He, J. N. Cutler, Y. Lu, and R. J. Bartlett, Phys. Rev. A **57**, 1906 (1998).
[5] J. P. Weightman, S. Cvejanović, and T. J. Reddish, J. Phys. B **31**, 1753 (1998).
[6] K. Soejima, A. Danjo, K. Okuno, and A. Yagishita, Phys. Rev. Lett. **83**, 1546 (1999).
[7] A. Huetz and J. Mazeau, Phys. Rev. Lett. **85**, 530 (2000).
[8] T. Weber, A. O. Czasch, O. Jagutzki, A. K. Müller, V. Mergel, A. Kheifets, E. Rotenberg, G. Meigs, M. H. Prior, S. Daveau *et al.*, Nature (London) **431**, 437 (2004).
[9] T. Weber, A. Czasch, D. Jagutzki, A. Müller, V. Mergel, A. Kheifets, J. Feagin, E. Rotenberg, G. Meigs, M. H. Prior *et al.*, Phys. Rev. Lett. **92**, 163001 (2004).
[10] T. Weber, Ph.D. thesis, Institut fuer Kernphysik, Frankfurt, 2003.
[11] M. Gisselbrecht, M. Lavollée, A. Huetz, P. Bolognesi, L. Avaldi, D. P. Seccombe, and T. J. Reddish, Phys. Rev. Lett. **96**, 153002 (2006).
[12] M. Brauner, J. S. Briggs, and H. Klar, J. Phys. B **22**, 2265 (1989).
[13] F. Maulbetsch and J. S. Briggs, J. Phys. B **26**, 1679 (1993).
[14] J. Berakdar and J. S. Briggs, Phys. Rev. Lett. **72**, 3799 (1994).
[15] I. Bray and A. T. Stelbovics, Phys. Rev. A **46**, 6995 (1992).
[16] I. Bray and D. V. Fursa, Phys. Rev. A **54**, 2991 (1996).
[17] I. Bray, Phys. Rev. Lett. **78**, 4721 (1997).
[18] A. Kheifets and I. Bray, J. Phys. B **31**, L447 (1998).
[19] P. Selles, L. Malegat, and A. K. Kazansky, Phys. Rev. A **65**, 032711 (2002).
[20] P. J. Marchalant and K. Bartschat, Phys. Rev. A **56**, R1697 (1997).
[21] F. Robicheaux, M. S. Pindzola, and D. R. Plante, Phys. Rev. A **55**, 3573 (1997).
[22] J. Colgan and M. S. Pindzola, J. Phys. B **34**, L457 (2001).
[23] J. Colgan and M. S. Pindzola, Phys. Rev. A **65**, 032729 (2002).
[24] M. Pont and R. Shakeshaft, Phys. Rev. A **51**, 494 (1995).
[25] C. W. McCurdy, D. A. Horner, T. N. Rescigno, and F. Martín, Phys. Rev. A **69**, 032707 (2004).
[26] J. Colgan, M. S. Pindzola, and F. Robicheaux, J. Phys. B **37**, L377 (2004).
[27] W. Vanroose, F. Martín, T. N. Rescigno, and C. W. McCurdy, Phys. Rev. A **70**, 050703(R) (2004).
[28] W. Vanroose, F. Martín, T. N. Rescigno, and C. W. McCurdy, Science **310**, 1787 (2005).
[29] W. Vanroose, D. A. Horner, F. Martín, T. N. Rescigno, and C. W. McCurdy, Phys. Rev. A **74**, 052702 (2006).
[30] D. A. Horner, W. Vanroose, T. N. Rescigno, F. Martín, and C. W. McCurdy, Phys. Rev. Lett. **98**, 073001 (2007).
[31] R. K. Peterkop, Opt. Spectrosc. **13**, 87 (1962).
[32] M. R. H. Rudge and M. J. Seaton, Proc. R. Soc. London **283**, 262 (1965).
[33] M. R. H. Rudge, Rev. Mod. Phys. **40**, 564 (1968).
[34] T. N. Rescigno, M. Baertschy, W. A. Isaacs, and C. W. McCurdy, Science **286**, 2417 (1999).
[35] C. W. McCurdy, M. Baertschy, and T. N. Rescigno, J. Phys. B **37**, R137 (2004).
[36] K. E. Banyard, J. Chem. Phys. **48**, 2121 (1968).
[37] S. A. Adelman, Phys. Rev. A **5**, 508 (1972).
[38] J. T. Broad and W. P. Reinhardt, Phys. Rev. A **14**, 2159 (1976).
[39] S. Leonardi and C. Calandra, J. Phys. B **26**, L153 (1993).
[40] M. A. Kornberg and J. E. Miraglia, Phys. Rev. A **49**, 5120 (1993).
[41] C. A. Nicolaides, C. Haritos, and T. Mercouris, Phys. Rev. A **55**, 2830 (1997).
[42] K. W. Meyer, C. H. Greene, and B. D. Esry, Phys. Rev. Lett. **78**, 4902 (1997).
[43] A. S. Kheifets and I. Bray, Phys. Rev. A **58**, 4501 (1998).
[44] M. S. Pindzola and F. Robicheaux, Phys. Rev. A **58**, 4229 (1998).
[45] E. Foumouo, G. L. Katma, G. Edah, and B. Piraux, Phys. Rev. A **74**, 063409 (2006).
[46] B. Simon, Phys. Lett. **71A**, 211 (1979).
[47] C. A. Nicolaides and D. R. Beck, Phys. Lett. **65A**, 11 (1978).
[48] C. W. McCurdy and F. Martín, J. Phys. B **37**, 917 (2004).
[49] T. N. Rescigno and C. W. McCurdy, Phys. Rev. A **62**, 032706 (2000).
[50] C. W. McCurdy, D. A. Horner, and T. N. Rescigno, Phys. Rev. A **63**, 022711 (2001).
[51] M. Baertschy, T. N. Rescigno, and C. W. McCurdy, Phys. Rev. A **64**, 022709 (2001).
[52] T. N. Rescigno, M. Baertschy, and C. W. McCurdy, Phys. Rev. A **68**, 020701(R) (2003).
[53] G. W. F. Drake, in *Atomic, Molecular and Optical Physics Handbook*, edited by G. W. F. Drake and N. E. Hedgecock (AIP, New York, 1996).
[54] M. Foster and J. Colgan, J. Phys. B **39**, 5067 (2006).